

# H-MoRe: Learning Human-centric Motion Representation for Action Analysis

Zhanbo Huang, Xiaoming Liu, Yu Kong

Department of Computer Science and Engineering, Michigan State University

{huang247}@msu.edu, {liuxm, yukong}@cse.msu.edu

## Abstract

In this paper, we propose *H-MoRe*, a novel pipeline for learning precise human-centric motion representation. Our approach dynamically preserves relevant human motion while filtering out background movement. Notably, unlike previous methods relying on fully supervised learning from synthetic data, *H-MoRe* learns directly from real-world scenarios in a self-supervised manner, incorporating both human pose and body shape information. Inspired by kinematics, *H-MoRe* represents absolute and relative movements of each body point in a matrix format that captures nuanced motion details, termed world-local flows. *H-MoRe* offers refined insights into human motion, which can be integrated seamlessly into various action-related applications. Experimental results demonstrate that *H-MoRe* brings substantial improvements across various downstream tasks, including gait recognition (CL@R1: 16.01% $\uparrow$ ), action recognition (Acc@1: 8.92% $\uparrow$ ), and video generation (FVD: 67.07% $\downarrow$ ). Additionally, *H-MoRe* exhibits high inference efficiency (34 fps), making it suitable for most real-time scenarios. Models and code is available at <https://github.com/haku-huang/h-more>.

## 1. Introduction

Understanding human motion has long been a fundamental challenge in computer vision. Leveraging motion information enables numerous practical applications, from rehabilitation [18, 22] in healthcare to video surveillance [38, 76] in security. This analysis relies on recognizing patterns in human motion, rather than the movement of irrelevant background elements (e.g., tree leaves). To enhance analysis performance, it is essential to extract precise human-centric motion that captures the nuances of human movement while suppressing irrelevant background dynamics.

Currently, human motion is commonly represented using two methods: optical flow and human pose. Optical flow captures motion between consecutive frames using a flow map to represent pixel motion offsets. It encodes both motion and shape information [2, 54] in a matrix format, mak-

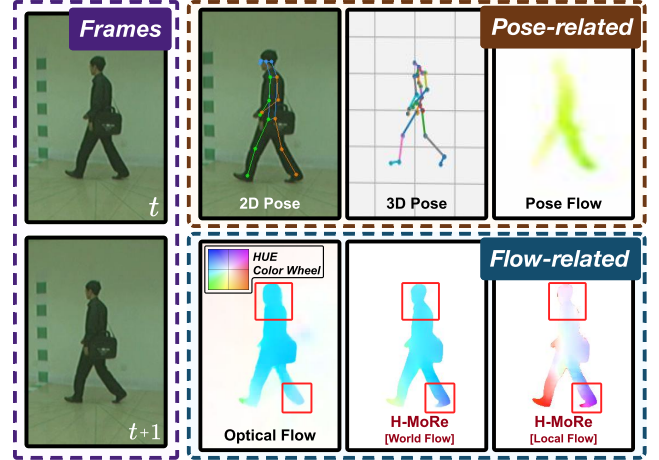


Figure 1. **Comparison of our H-MoRe with other motion representations.** We visualize three pose-related representations – 2D Pose [16], 3D Pose [41], and PoseFlow [66] – as well as flow-related representations: Optical Flow [47], and our H-MoRe (contains world flow and local flow). The red box highlights H-MoRe’s precise motion information and sharp boundaries.

ing it easily perceptible by Convolutional Neural Networks (CNNs) or Vision Transformers (ViTs). As a result, optical flow has become a popular input signal for action recognition [3, 37, 45] and video generation [26, 55, 61]. However, it calculates offsets indiscriminately for all pixels, which is inadequate for human-centric scenarios with moving backgrounds. Additionally, optical flow learned from synthetic datasets lacks real biological entities [28, 35, 50] and struggles to capture subtle nuances of human motion. Consequently, recent analysis tasks [32, 65] have shifted to using human pose, which represents motion through 2D [30, 62] or 3D skeletal points [4, 71, 74]. However, human pose lacks body shape information, which is particularly important for specific tasks such as gait recognition [11, 77].

To address these challenges, we propose **H-MoRe**, a new formulation for **Human-centric Motion Representation** that accurately preserves both the motion and shape information of the human body. Unlike the Endpoint Error (EPE) [17], a common objective function for fully-supervised opti-

cal flow estimation, we learn H-MoRe directly from real-world scenarios through a *joint constraint learning framework*, which incorporates two self-supervised constraints – a skeleton constraint and a boundary constraint – to capture accurate motion and shape information, respectively. The skeleton constraint establishes associations between each body point and the skeleton, allowing H-MoRe to use skeleton offsets to approximate the range of body motion. Meanwhile, the boundary constraint refines human motion in local regions, such as hands and feet, and ensures that H-MoRe captures the overall body shape. This is achieved by aligning the edges in our representation with human boundaries during training. The *joint constraint learning framework* enables H-MoRe to enhance performance across various human-centric tasks that heavily rely on motion and shape information, such as gait recognition [14, 33, 63, 68], action recognition [12, 34, 69], and video generation [21, 23, 67].

Additionally, while most motion representations depict human movement within an environmental context, certain tasks [20, 70, 72] require focused analysis of specific body parts, *e.g.*, the left arm. Drawing on principles of physical kinematics, H-MoRe introduces local flow to represent movements relative to the subject, highlighting intrinsic motion details. Combined with world flow, which captures the movement of each body point relative to the environment, this *world-local flows* provides a more comprehensive and nuanced representation of human motion, incorporating both absolute and relative movement information for downstream tasks.

Fig. 1 highlights the unique features of our world-local flows. By visualizing flow using the HUE color wheel [5], we can clearly see that world flow captures motion details with exceptional clarity, including body boundaries and finer points like foot movement – outperforming existing methods. Meanwhile, local flow reveals the distinctive qualities of local flow, with a richer color spectrum indicating more detailed underlying motion information. This self-referential flow provides unique insights for downstream tasks involving human motion.

Our contributions are summarized as follows:

1. We introduce an innovative pipeline, termed H-MoRe, which provides a human-centric motion representation with precise motion and shape information, easily integrable into any motion analysis algorithms.
2. We design the *joint constraint learning framework*, enabling the estimation model to learn human motion from any real-world sequences without ground truth.
3. We propose *world-local flows*, which capture absolute and relative motions and provide richer insights about human-centric motion for practical analysis tasks.
4. Extensive experiments on three distinct analysis tasks demonstrate the superiority of our H-MoRe in enhanc-

ing the performance of various action analysis tasks.

## 2. Related Work

### 2.1. Learning Methods of Optical Flow

Initially, optical flow estimation is formulated as an energy minimization problem [25]. This problem is constructed using such combined regularization terms by assuming that moving objects maintain the same brightness across frames and the flow is smooth between adjacent pixels. Subsequently, with the development of CNNs, the Endpoint Error (EPE) is introduced to calculate the Euclidean distance between predicted and ground truth at the pixel level. Many optical flow estimation methods use EPE as the supervisory signal at single [13] or multiple scales [44, 47]. Recently, thanks to the global information extraction capability of Transformers, some methods [27, 56] construct loss functions based on the matching cost between each pixel pair in the feature space, termed Cost Volume Loss. It is calculated by measuring the deviation between the minimum cost location in the cost volume and ground truth. Further, FlowFormer++ [43] enhances the model’s understanding of global features by applying a masking mechanism to the cost volume. However, these pixel-level loss functions are often ineffective in estimating human-centric motion. Thus, exploring a human-centric learning framework to learn human motion from real-world scenarios is particularly desirable. To address this, we propose the *joint constraint learning framework*, which enables H-MoRe to learn to extract precise human motion in a self-supervised manner from any human sequences.

### 2.2. Human-centric Motion Representation

Researchers have explored various approaches to describing human motion for improving the performance of downstream tasks such as action recognition. As an explicit motion representation, optical flow is widely used as an additional input channel to capture motion information [7, 10]. However, as action analysis tasks have advanced, the complexity of human motion makes it increasingly difficult to extract useful information from optical flow. Since optical flow is a non-human-oriented representation, it struggles to meet the specific demands of human motion analysis. Consequently, many analysis systems turn to extract implicit human motion from pose information. They employ GNNs to analyze the relationship between skeletal keypoints in each frame [48, 58]. Early on, these skeletal keypoints are commonly detected by CNNs [6, 24, 57]. They represent the earliest human-centric motion representations. With advancements in 3D computer vision, models like VideoPose3D [36] and MotionBERT [75] leverage temporal cues to improve the accuracy of pose estimation at each moment. However, although pose information is

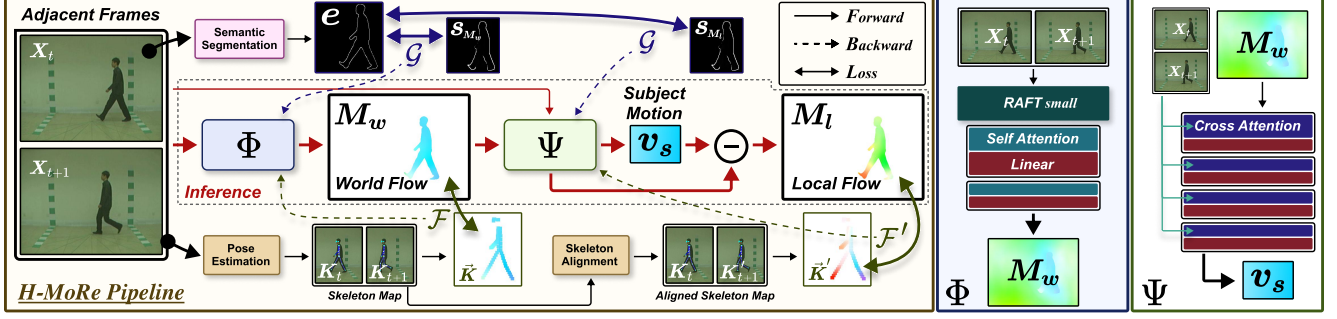


Figure 2. **Whole Pipeline of H-MoRe.** From left to right: (a) The training and inference pipeline for *world-local* flows (outlined by a gray dashed line) and the use of the *joint constraints learning framework* for self-supervised learning from real-world scenarios. Blue symbols and lines denote the boundary constraint  $\mathcal{G}$ , while green symbols and lines indicate the skeleton constraint  $\mathcal{F}$ . Backpropagation gradients are shown as dashed lines in corresponding colors; (b) the internal implementation of  $\Phi$ ; and (c) the internal implementation of  $\Psi$ .

sufficiently accurate, it overlooks the role of shape information in analysis tasks. For example, gait recognition relies on the motion of specific body parts to identify a person, and the absence of the human shape makes pattern matching challenging. Therefore, it is important to represent complex human motion while preserving the integrity of the human shape. Motivated by this challenge, we introduce *world-local* flows, which extract motion information across two distinct reference systems, providing a clear delineation of human boundaries and thereby enhancing the performance of various downstream tasks.

### 3. Methodology

#### 3.1. Method Overview

Motion representation is commonly computed by estimating optical flow. However, the estimated flow map represents both background and foreground motion, with human motion often obscured in the noisy map and thus challenging to use for downstream human action analysis tasks. In this paper, we propose a human-centric motion representation and demonstrate its benefits for these tasks. A complete list of symbols is provided in the Appendix (Tab. 7).

As shown in Fig. 2, our method learns human-centric motion representations from perspectives: human motion relative to the environment, termed world flow  $M_w$ , and motion relative to the human subject, termed local flow  $M_l$ . Together, these *world-local* provide comprehensive motion information for downstream tasks.

To begin, given two consecutive frames  $X_t$  and  $X_{t+1}$ , we utilize a network  $\Phi$  to calculate a flow map as  $M_w = \Phi(X_t, X_{t+1}; \omega_1)$ , where  $\omega_1$  denotes the network parameters. To obtain the optimal world flow  $M_w$  with precise motion and detailed shape information, *i.e.*, to optimize  $\omega_1$ , we propose a *joint constraint learning framework* that learns from real-world scenarios in a self-supervised manner. The proposed learning framework has two fidelity

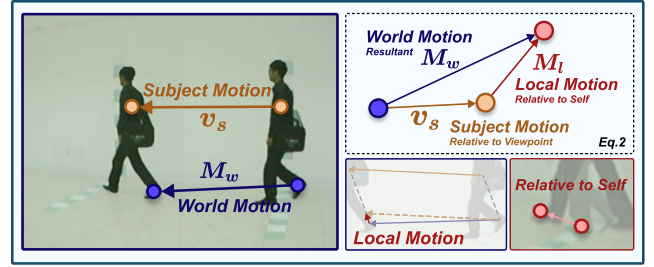


Figure 3. **Definition of world-local flows.** World motion  $M_w$  is movement relative to the environment, while local motion  $M_l$  is relative to the subject. Using the subject’s overall motion  $v_s$ , these can be converted via vector composition and decomposition.

terms: the skeleton constraint  $\mathcal{F}$  and the boundary constraint  $\mathcal{G}$ . The skeleton constraint  $\mathcal{F}$  uses pose information to ensure that each body point’s movement adheres to kinematic constraints. Specifically,  $\mathcal{F}$  quantifies the discrepancy between the estimated flow map  $M$  and the skeleton offset between the poses in frames  $X_t$  and  $X_{t+1}$ . To further incorporate body shape and fine-grained motion, the boundary constraint  $\mathcal{G}$  aligns human shapes onto the flow map by measuring the Chamfer distance between human boundaries in estimated flow  $M$  and frame  $X_t$ . Our world flow  $M_w$  is then defined as:

$$M_w = \arg \min_M [\mathcal{F}(M, X_t, X_{t+1}) + \alpha \cdot \mathcal{G}(M, X_t)], \quad (1)$$

where  $\alpha$  balances the contributions of each term. Details of  $\mathcal{F}$  and  $\mathcal{G}$  are discussed in Sec. 3.2.

Although world flow  $M_w$  is effective, certain tasks require a focus on motion relative to the subject. In these scenarios, subject-relative motion (*e.g.*, the arm’s movement relative to the body) becomes more critical than motion relative to the environment. We refer to this subject-relative motion as local flow  $M_l$ .

The estimation of local flow  $M_l$  can theoretically be

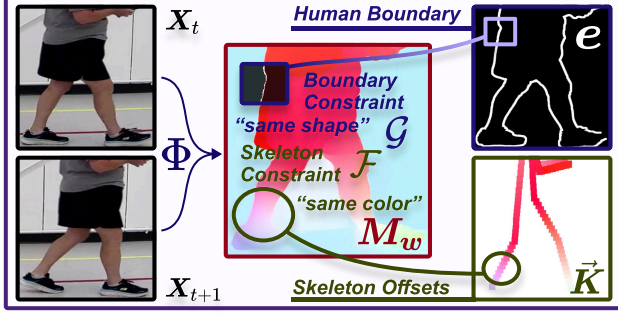


Figure 4. **Overview of joint constraint learning framework.** We introduce two constraints – (1) the boundary constraint  $\mathcal{G}$  (blue), which aligns the human boundary with the flow edges to maintain consistent shapes; and (2) the skeleton constraint  $\mathcal{F}$ , which uses skeleton offsets to regulate body point movements, ensuring consistent motion, as reflected by matching colors in the visualization.

achieved using the same network architecture as that used for world flow  $M_w$ . However, this would double the inference time for H-MoRe, violating the requirement for real-time downstream tasks. Inspired by Galilean transformations [19] in kinematics, we identify a connection between world flow  $M_w$  (blue vector) and local flow  $M_l$  (red vector), as shown in Fig. 3. This allows us to avoid using a separate network  $\Phi'$  to estimate  $M_l$ . Instead, we employ a lightweight network  $\Psi$  to estimate the subject’s overall motion trend  $v_s$  (brown vector) based on  $M_w$ . By applying vector decomposition, as shown in Fig. 2, we can estimate local flow  $M_l$  indirectly with lower computational cost:

$$\begin{aligned} v_s &= \Psi(X_t, X_{t+1}, M_w; \omega_2), \\ M_l &= M_w - v_s, \end{aligned} \quad (2)$$

where  $\omega_2$  denotes the network parameters. Our joint constraint learning framework is similarly applied to  $M_l$ , as detailed in Sec. 3.3.

### 3.2. Joint Constraint Learning Framework

We discuss the skeleton constraint  $\mathcal{F}$  and the boundary constraint  $\mathcal{G}$  in Eq. (1) for world flow  $M_w$  in the following, and adapt them to local flow  $M_l$  in Sec. 3.3.

#### 3.2.1. Skeleton Constraint

To define the overall range of motion for H-MoRe, we use pose information to establish a dynamic relationship between the skeleton and body.

Using 2D pose estimation (e.g., ED-Pose [59]), we extract 17 joint points from frames  $X_t$  and  $X_{t+1}$ , each with corresponding coordinates and visibility  $c$ . By uniformly sampling joint-related  $n_k$  points along each bone segment, we interpolate these joint points to construct a skeleton map  $K_t$  and subsequently calculate the skeleton offsets  $\vec{K} = K_{t+1} - K_t$  (as shown in Fig. 2 and Fig. 4).

To constrain body motion using skeletal offsets, as shown in Fig. 5 (a), for any body point  $p$  (red point), we identify the closest skeletal keypoint  $\hat{q}$  (blue point) with the highest visibility. This matching process is defined as:

$$\hat{q} = \arg \min_{q \in K_t \odot S} (-\|p - q\| \times \log c_q), \quad \text{s.t. } p \in M \odot S, \quad (3)$$

where  $c_q$  is the visibility of  $q$ . The  $\odot S$  operation restricts matching to the subject region  $S$ , preventing incorrect voxel matches in flow  $M$  when multiple subjects are present.

Given the matched body-skeleton pair  $\langle p, \hat{q} \rangle$ , we apply the skeletal offset at  $\hat{q}$  in  $\vec{K}$ , denoted as  $k_{\hat{q}}$  (blue vector), to constrain the estimated flow  $M$  at  $p$ , denoted as  $u_p$  (red vector). Guided by the kinematic constraints of the human body, we assume that  $u_p$  should be neither orthogonal to  $k_{\hat{q}}$  nor significantly different in motion intensity. To enforce these properties, we define the skeleton constraint  $\mathcal{F}$  with two sub-constraints: an angular constraint  $\mathcal{F}_A$  and an intensity constraint  $\mathcal{F}_I$ .

As shown in Fig. 5 (b), we define the angular constraint  $\mathcal{F}_A$  by calculating the angle between  $u_p$  and  $k_{\hat{q}}$ . We establish ideal (green sector) and excessive (red sector) motion ranges based on a empirically specified threshold  $\vartheta_a$ , as:

$$\mathcal{F}_A(u_p, k_{\hat{q}}) = \mathbb{I} \left( \frac{u_p \cdot k_{\hat{q}}}{\|u_p\| \cdot \|k_{\hat{q}}\|} \geq \vartheta_a \right), \quad (4)$$

where  $\mathbb{I}(\cdot)$  is an indicator function that identifies body points with abnormal motion.

Similarly, we expect the motion intensity of a body point to be consistent with that of its corresponding skeletal point. As shown in Fig. 5 (c), we define the intensity constraint  $\mathcal{F}_I$  by establishing an acceptable intensity range (green ring) and error ranges for low or high intensities (red circle and ring). When  $u_p$  falls outside the green ring, a penalty is applied:

$$\mathcal{F}_I(u_p, k_{\hat{q}}) = \text{ReLU}[(\|u_p\| - \vartheta_i^l \cdot \|k_{\hat{q}}\|) \cdot (\|u_p\| - \vartheta_i^h \cdot \|k_{\hat{q}}\|)] \quad (5)$$

By applying both angular and intensity sub-constraints, we bind each body point’s motion to skeletal motion, precisely defining the feasible movement range for each point. The complete skeleton constraint  $\mathcal{F}$  in Eq. (1) is thus:

$$\mathcal{F} = \frac{1}{h \cdot w} \sum_{p \in M} [\mathcal{F}_A(u_p, k_{\hat{q}}) + \beta \cdot \mathcal{F}_I(u_p, k_{\hat{q}})], \quad (6)$$

where  $\beta$  balances the angular and intensity sub-constraints.

#### 3.2.2. Boundary Constraint

To refine motion details and incorporate shape information, we use human boundaries  $e$  as a prior to ensure that the learned flow  $M$  closely adheres to the human body.

As illustrated in Fig. 5 (d), we minimize the Chamfer distance [1, 64] between the human boundaries  $e$  and flow



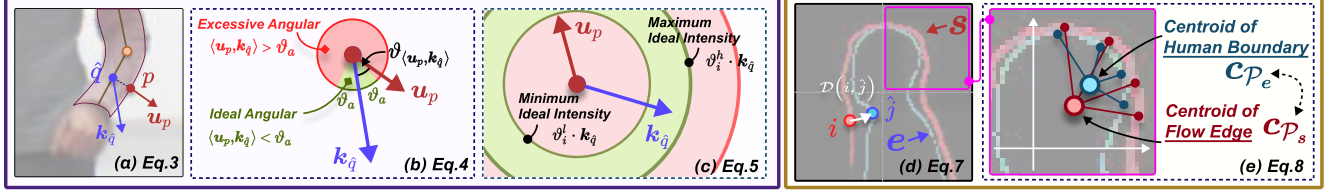


Figure 5. **Details of our joint constraint.** (a) matching any body point  $p$  to its corresponding skeleton point  $\hat{q}$ ; (b) an angular constraint to align estimated motion with skeleton’s movement directions; (c) an intensity constraint to ensure consistent motion magnitude between estimated motion and skeleton offsets; (d) matching any point  $i$  on the flow edges  $s$  to its corresponding  $\hat{j}$  on human boundaries  $e$ ; and (e) calculation of our patch-centroid distance.

edges  $s$ . Human boundaries are detected using a Canny operator on the semantic segmentation results (e.g., from U<sup>2</sup>Net [39]), while flow edges are obtained from our custom algorithms detailed in the appendix. This distance is defined as the sum of the nearest distances from each point  $i$  (red point) on the flow edges  $s$  (red curve) to  $e$  (blue curve):

$$\mathcal{C}(s, e) = \sum_{i \in s} \mathcal{D}(i, \hat{j}), \text{ s.t. } \hat{j} = \arg \min_{j \in e} \mathcal{D}(i, j), \quad (7)$$

where  $\mathcal{D}(\cdot)$  is the Euclidean distance between two points.

Directly matching points between the two dense curves  $e$  and  $s$  is computationally expensive. For efficiency, we propose *patch-centroid distance*, which approximates Chamfer distance via matrix operations. Specifically, we divide both  $e$  and  $s$  into patches at multiple scales by applying kernels of varying receptive fields as shown in Fig. 5 (e). For each patch  $\mathcal{P}$ , the Chamfer distance between curves within that patch ( $\mathcal{P}_s$  and  $\mathcal{P}_e$ ) is approximated by calculating the distance between their centroids  $c$  (large red and blue points), assuming a smooth distribution of points:

$$\mathcal{C}(\mathcal{P}_s, \mathcal{P}_e) = \frac{1}{n_p} \sum_{\{i, \hat{j}\}} \mathcal{D}(i, \hat{j}) \approx \mathcal{D}(c_{\mathcal{P}_s}, c_{\mathcal{P}_e}), \quad (8)$$

where  $n_p$  is the total number of point pairs in each patch, while the  $\{i, \hat{j}\}$  represents all matching pairs of  $\langle i, \hat{j} \rangle$ . The derivation of this approximation and its experimental validation are provided in the appendix.

To improve the accuracy of the approximation, we further divide patches and calculate patch-centroid distances at multiple scales. Thus, the boundary constraint  $\mathcal{G}$  is:

$$\mathcal{G} = \frac{1}{n_{ms}} \sum_{ms} \left[ \frac{1}{n_p} \sum_{\mathcal{P} \propto ms} \mathcal{C}(\mathcal{P}_s, \mathcal{P}_e) \right], \quad (9)$$

where  $n_{ms}$  is the number of scales and  $n_p$  is the number of patches at scale  $ms$ .

### 3.3. World-Local Flow Estimation

Given the definitions of world-local flows in Sec. 3.1, H-MoRe operates in two stages. First, we directly estimate

world flow  $M_w$ . Then, we indirectly compute local flow  $M_l$  by estimating subject motion  $v_s$ :  $M_l = M_w - v_s$  from Eq. (2).

We estimate world flow  $M_w$  between frames using flow estimation network  $\Phi$ , whose backbone could be any optical flow estimation networks, e.g., RAFT [44] or FlowFormer [27]. To reduce carbon emissions during training H-MoRe from scratch, we use RAFT-small as the backbone in  $\Phi$  in our experiments. Additionally, as shown in Fig. 2, we add two self-attention blocks to emphasize human-centric motion and filter out irrelevant information to motion analysis. In training, the joint constraints in Sec. 3.2 guide the optimization of  $\omega_1$  in  $\Phi$ .

As described in Eq. (2), we use a lightweight network  $\Psi$  to estimate subject motion  $v_s$  based on world flow  $M_w$  and input frames. Our implementation of  $\Psi$  includes cross-attention blocks with a depth of 4.

During training, we use Eq. (1) to optimize the parameters  $\omega_1$  in  $\Phi$  to obtain the world flow  $M_w$ . However, since the skeleton offset at point  $\hat{q}$  ( $k_{\hat{q}}$ ) in  $\mathcal{F}$  (Eq. (6)) represents movement relative to the environment, this constraint cannot be directly applied to the learning process of the local flow  $M_l$ , i.e., it cannot be used to optimize  $\omega_2$  in  $\Psi$ .

To address this issue, we adjust the skeleton constraint ( $\mathcal{F}$ ). Specifically, before computing the difference between the two skeleton maps  $K_t$  and  $K_{t+1}$ , we first align  $K_{t+1}$  to  $K_t$ , termed  $K'_{t+1}$ . This alignment can be achieved in various ways, e.g., solving a homography matrix by analytical solution or using head-based alignment. Consequently, we obtain  $\vec{K}'$ , and then replacing  $k_{\hat{q}}$  with  $k'_{\hat{q}}$  in Eq. (4) and Eq. (5). This results in a subject-relative constraint  $\mathcal{F}'$ . Through this, we can determine the optimal  $\omega_2$  in Eq. (2).

## 4. Experiments

To evaluate the benefits of using H-MoRe as a motion representation for downstream tasks, we select three representative human-centric motion related tasks: gait recognition, action recognition, and video generation. Our evaluation is conducted on three datasets: CASIA-B [73], Diving48 [31], and UTD-MHAD [9]. From each dataset’s training set, we

Methods	Efficiency Analysis		GaitBase [Params: 34.2M]			GaitSet [Params: 6.3M]		
	Params (M)	FLOPs (G)	NM@R1↑	BG@R1↑	CL@R1↑	NM@R1↑	BG@R1↑	CL@R1↑
w/o Flow	-	-	96.51	91.50	78.02	92.82	82.25	69.24
RAFT [47]	5.25	1780.4	96.91	93.12	80.52	93.28	82.21	70.55
GMA [29]	5.88	2450.3	96.61	92.83	83.63	<u>93.72</u>	83.33	71.64
GMFlow [56]	4.68	428.6	97.72	93.59	85.22	93.62	<u>83.82</u>	<u>72.75</u>
CRAFT [44]	6.30	4204.7	96.27	92.60	79.61	93.71	82.89	71.12
SKFlow [46]	6.27	2731.5	96.59	92.42	82.13	93.52	82.38	70.53
VideoFlow [42]	12.65	3159.3	<u>97.88</u>	94.01	<u>86.12</u>	93.55	82.59	70.73
FlowFormer++ [43]	16.15	3048.1	96.66	<u>94.31</u>	85.70	93.65	83.35	71.75
<b>H-MoRe Ours</b>	5.57	861.5	<b>98.26</b>	<b>95.62</b>	<b>87.66</b>	<b>98.27</b>	<b>94.46</b>	<b>85.25</b>

Table 1. **Quantitative comparison for gait recognition.** Using GaitBase [15] and GaitSet [8] (for real-time scenarios) as gait recognition models, we compare H-MoRe against seven optical flow estimation methods on the CASIA-B dataset. Higher values indicate better performance across all metrics. The best result is highlighted in **bold**, and the second-best is underlined. The left two columns present an efficiency comparison of these flow estimation algorithms using the total parameters and FLOPs.

sample 2, 800, 14, 000, and 600 sequences, respectively, to train H-MoRe. For each sequence, we extract 16 frames (8 frames for Diving48) and resize them to  $512 \times 384$ .

We set the tuning parameters  $\alpha$  and  $\beta$  to 0.1 and 0.01, and define the thresholds  $\vartheta_a$ ,  $\vartheta_i^l$ , and  $\vartheta_i^h$  as  $15^\circ$ , 0.8, and 1.2, respectively. All learnable parameters are optimized using AdamW optimizer with a learning rate of  $1.0 \times 10^{-4}$  and exponential decay. Training is conducted over 8 epochs with a batch size of 64. Our approach is implemented in PyTorch and runs on 16 NVIDIA RTX 6000 Ada GPUs.

#### 4.1. Results on Gait Recognition

Gait recognition is the task of identifying individuals based on unique walking patterns, where human motion is an important cue. The CASIA-B dataset includes videos of 124 individuals recorded from 11 viewpoints under three conditions: normal walking (NW), bag carrying (BG), and clothing change (CL). The primary challenge in this task is to accurately recognize individuals despite variations in appearance, making precise motion information essential.

Rank-1 (R1) accuracy measures the percentage of times the model’s top prediction matches the correct label. We use GaitBase [15] as the gait recognition model to evaluate H-MoRe’s ability to integrate with complex downstream networks. The inputs to GaitBase are per-frame silhouettes and flow (optical flow or H-MoRe) between consecutive frames.

As shown in Tab. 1, under both NM and BG conditions, the model using H-MoRe as the motion representation achieves higher R1 accuracy compared to models using optical flow. The CL condition is the most challenging in gait recognition, as clothing changes make it difficult to rely on body or clothing shape for identification. In this case, accurate motion information is essential. The GaitBase model, leveraging motion information from H-MoRe, achieves top accuracy, showing a 9.64% improvement over

Methods	Action Rec. [Diving48]		Video Gen. [MHAD]	
	Acc@1↑	Acc@5↑	SSIM ↑	FVD ↓
w/o Flow	64.07	95.08	0.9463	329.22
RAFT	65.90	95.42	0.9557	118.13
GMA	69.00	95.62	<u>0.9565</u>	<u>114.98</u>
GMFlow	<u>71.74</u>	95.51	0.9529	429.82
CRAFT	71.24	95.85	0.9532	424.72
SKFlow	71.39	96.64	0.9541	325.08
VideoFlow	71.45	<u>96.72</u>	0.9564	165.63
FlowFormer++	64.28	95.88	0.9553	284.95
<b>H-MoRe Ours</b>	<b>72.99</b>	<b>97.62</b>	<b>0.9574</b>	<b>108.38</b>

Table 2. **Quantitative comparison for action recognition and video generation.** For action recognition, higher metric values indicate more accurate classification. In video generation, higher SSIM [52] scores reflect better frame quality, while lower FVD [49] scores indicate that the generated video more closely resembles real footage.

the models that do not incorporate flow (87.66 vs 78.02).

Furthermore, to evaluate H-MoRe in real-time applications, we use a lightweight model, GaitSet [8]. As the motion representation, H-MoRe provides a 12.50% gain (CL@R1) over GaitSet using optical flow, underscoring H-MoRe’s advantage in real-time gait recognition.

#### 4.2. Results on Action Recognition

Action recognition is widely used to classify human motion into categories, such as running and walking. To evaluate H-MoRe’s capability in multi-person and high-speed scenarios, we test it on the Diving48 dataset, which contains approximately 18, 000 sequences covering 48 types of diving actions. A primary challenge in Diving48 is that most dives occur within 2 seconds, often resulting in significant



Figure 6. **Qualitative comparison of video generation.** Results of LGC-VD using RAFT and our H-MoRe as motion conditions. We show the generated first frame ( $1^{st}$ ) and last frame ( $15^{th}$ ) and corresponding ground truth (GT).

motion blur across frames.

We use Acc@1 and Acc@5 as metrics, which measure the percentage of times the model’s top-1 and top-5 predictions match the correct label, respectively. VideoFocalNets [53] is used as the action classifier, with frames and different flows (optical flow or H-MoRe) as inputs. These models are trained from scratch on the same dataset to ensure experimental fairness.

As shown in Tab. 2, the model using H-MoRe as the motion representation achieves a notable improvement in Acc@5 (0.9%  $\uparrow$ ), indicating enhanced robustness. This improvement is attributed to our *joint constraint learning framework*, which is specifically designed for human-centric scenarios, making H-MoRe less susceptible to challenges such as subject overlap, motion blur, and noisy backgrounds. Additionally, we observe a substantial advantage in Acc@1, with an 8.92% improvement over the baseline model without any flow, due to H-MoRe’s precise motion information.

Given the real-time requirements of practical scenarios, such as sports events, we conduct experiments using TSN [51] as a more lightweight action classifier in place of VideoFocalNets. In this setup, using our method as the motion representation yields a more pronounced improvement Acc@1 (1.67% $\uparrow$ ). Detailed results are in the appendix.

### 4.3. Results on Video Generation

Understanding motion is essential for effective video generation. To access whether H-MoRe can provide accurate motion information for video generation models, we conduct experiments on the UTD-MHAD dataset. This dataset includes 861 action sequences spanning 27 action types performed by 8 subjects, with each action repeated 4 times.

We use SSIM [52] and FVD [49] as metrics. SSIM measures the spatial consistency between generated and real videos at the frame level, reflecting the quality of generated frames. FVD evaluates the consistency between generated and real videos in high-dimensional feature space, capturing the dynamic coherence and realism of the video.

We use LGC-VD [60] as the generation model, taking the first two frames as input and using flows from various methods as conditioning information. As shown in Tab. 2, compared to generation models using optical flow, the model with H-MoRe achieves a higher SSIM (0.25% $\uparrow$ )

Constraint		Gait Rec.			Action Rec.	
$\mathcal{F}$	$\mathcal{G}$	NM@R1 $\uparrow$	BG@R1 $\uparrow$	CL@R1 $\uparrow$	Acc@1 $\uparrow$	Acc@5 $\uparrow$
$\checkmark$		97.15	91.47	83.01	72.13	96.14
	$\checkmark$	96.99	93.09	84.93	68.17	95.23
$\checkmark$	$\checkmark$	<b>98.26</b>	<b>95.62</b>	<b>85.25</b>	<b>72.99</b>	<b>97.62</b>

Table 3. **Ablation study on joint constraint.** Quantitative comparison results on gait recognition and action recognition.

and lower FVD (5.74% $\downarrow$ ). As illustrated in Fig. 6, in the first and last frames generated by models conditioned on RAFT, noticeable distortions or missing appear in hands and head (marked with red boxes). This degradation occurs because optical flow inaccurately estimates human and environmental motion, resulting in unclear body shapes and causing generation models to struggle with retaining texture details. In contrast, our H-MoRe is tailored for human-centric scenarios, and ensures high generation quality.

### 4.4. Qualitative Comparison

In Fig. 7, we present a qualitative comparison of H-MoRe’s *world-local flows* on the CASIA-B dataset, highlighting the distinctions between our method and optical flow estimation methods. The zoom-in regions show H-MoRe’s advantages: thanks to the skeleton constraint, our method provides more accurate overall motion. Additionally, the boundary constraints allow for precise human edge details in areas such as the head and feet. Most importantly, the unique representation of local flow further underscores the underlying motion information, setting it apart from other methods.

### 4.5. Ablation Studies

**Study on Joint Constraint** We ablate the effects of the two constraints in H-MoRe. Tab. 3 and Fig. 8 show the results when each constraint is applied individually. Using only the skeleton constraint  $\mathcal{F}$  aligns motion direction and magnitude but introduces unintended motion information, as shown by the red box in Fig. 8. In contrast, applying only the boundary constraint  $\mathcal{G}$  yields precise human edges but leads to substantial errors in motion information. Combining two constraints results in a representation that accurately captures both precise motion and shape details, optimizing H-MoRe for human-centric motion representations.

**Study on World-Local Flows** To analyze the unique characteristics of our *world-local flows*, we conduct experiments using only world flow  $M_w$  or local flow  $M_l$  on gait recognition and action recognition tasks. As shown in Tab. 4, results indicate that using only local flow  $M_l$  generally achieves higher accuracy than using world flow  $M_w$  alone, supporting our assertion in Sec. 3.1 that certain tasks

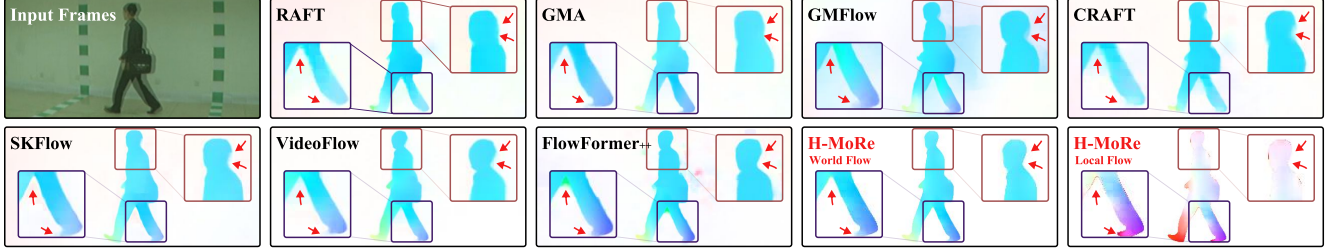


Figure 7. **Qualitative comparison of flow visualizations.** Flow visualizations generated by our H-MoRe and seven SoTA optical flow estimation algorithms on the same frame pair. Primary differences are marked and zoomed with red boxes and arrows.

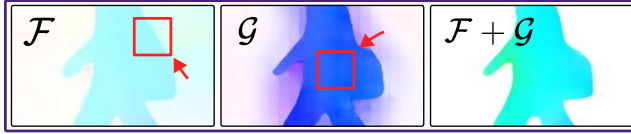


Figure 8. **Ablation study on joint constraint.** Visual comparison of motion estimation results using individual constraints versus joint constraints.

W-L Flows		Gait Rec.			Action Rec.	
$M_w$	$M_l$	$NM@R1\uparrow$	$BG@R1\uparrow$	$CL@R1\uparrow$	$Acc@1\uparrow$	$Acc@s\uparrow$
✓		97.13	92.31	80.78	70.91	95.79
	✓	98.13	94.41	82.82	72.64	95.38
✓	✓	<b>98.26</b>	<b>95.62</b>	<b>85.25</b>	<b>72.99</b>	<b>97.62</b>

Table 4. **Ablation study on world-local flows.** Quantitative comparison results on gait recognition and action recognition.

rely more on motion relative to the subject than the environment. More importantly, combining both flows, *i.e.*, *world-local flows*, yields higher accuracy than either world or local alone, highlighting their complementary nature. This combination provides more insightful motion representations for human-centric action analysis, as demonstrated in Tab. 1 and Tab. 2.

#### 4.6. Comparison with Pose Estimation Methods

As mentioned in Sec. 1, optical flow and human pose are two common motion representations. Since all baselines in Tab. 1 and Tab. 2 are optical flow estimation methods, we now compare H-MoRe with models that use pose as the motion representation, including 2D pose from AlphaPose [16] and 3D pose from MotionBERT [75]. In the comparisons in previous subsections, all flows are used as additional input channels, concatenated with silhouettes (for gait recognition) or frames (for action recognition). Because CNNs and ViTs cannot directly process pose information, in this subsection we use ST-GCN [58] to extract motion features from the pose data. These features are then fused with visual features extracted by CNNs or ViTs through cross-attention

Representation	Gait Rec.			Action Rec.	
	$NM@R1\uparrow$	$BG@R1\uparrow$	$CL@R1\uparrow$	$Acc@1\uparrow$	$Acc@s\uparrow$
2D Pose [~25M]	96.82	93.44	82.17	70.66	96.11
3D Pose [~41M]	97.21	94.32	84.05	71.51	97.09
<b>H-MoRe [~5.7M]</b>	<b>98.26</b>	<b>95.62</b>	<b>87.66</b>	<b>72.99</b>	<b>97.62</b>

Table 5. **Quantitative comparison with pose-based models.** Performance of gait and action recognition using pose information versus H-MoRe as the motion representation.

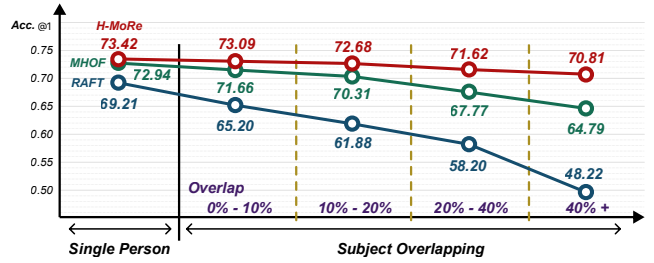


Figure 9. **Robustness with increasing subject overlap.** As subject overlap increases, action recognition model’s accuracy using H-MoRe (red) decreases more slowly than others.

layers and used as input to the classification head.

As shown in Tab. 5, H-MoRe achieves significantly higher accuracy across all three settings in gait recognition, due to the additional shape information we provide.

#### 4.7. Robustness for Overlapping Subjects

We evaluate H-MoRe’s robustness in scenarios with overlapping subjects. Based on the degree of bounding box overlap between subjects, we divide Diving48 into five bins, ranging from no overlap to 40% overlap, as shown in Fig. 9. Since RAFT is not designed with a human-centric motivation, it struggles to distinguish pixels from multiple subjects. As overlap levels increase, the accuracy of classifiers using RAFT (blue line) as the motion representation declines rapidly. We also compare against MHOE [40], which was trained under supervision on a synthetic multi-person dataset. Due to its lack of exposure to real-world high-speed motion, classifiers using MHOE (green line) exhibit a no-



ticeable performance drop once the subject overlap exceeds 20%. In contrast, H-MoRe, tailored for human-centric scenarios, mitigates the impact of increasing overlap, resulting in a significantly slower decline in accuracy.

## 5. Conclusion

In this paper, we introduce H-MoRe, a novel pipeline designed to enhance the precision of human-centric motion analysis. Through a *joint constraint learning framework* and motion representation across two distinct reference systems, *i.e.*, *world-local flows*, our method provides deeper insights into human motion. Experimental results show that our method substantially improves performance across diverse downstream tasks. Due to computational constraints, our approach is primarily validated in 2D with a limited number of subjects. Future work should aim to extend this framework to 3D environments and more complex multi-subject scenarios, potentially increasing H-MoRe’s applicability and accuracy in real-world applications.

## Acknowledgment

This research is partially supported by the Army Research Office (ARO) grant W911NF-24-1-0385, the Office of Naval Research (ONR) grant N00014-23-1-2046, and the Office of the Director of National Intelligence (ODNI), Intelligence Advanced Research Projects Activity (IARPA), via 2022-21102100004. The views and conclusions contained in this document are those of the authors and should not be interpreted as necessarily representing the official policies, either expressed or implied, of ARO, ONR, ODNI, IARPA, or the U.S. Government. The U.S. Government is authorized to reproduce and distribute reprints for governmental purposes notwithstanding any copyright annotation therein.

## References

- [1] Yasuhiro Aoki, Hunter Goforth, Rangaprasad Arun Srivatsan, and Simon Lucey. Pointnetlk: Robust & efficient point cloud registration using pointnet. In *Proceedings of the IEEE/CVF Conference on Computer Vision and Pattern Recognition (CVPR)*, pages 7163–7172, 2019. 4
- [2] Simon Baker, Daniel Scharstein, James P Lewis, Stefan Roth, Michael J Black, and Richard Szeliski. A database and evaluation methodology for optical flow. *International Journal of Computer Vision (IJCV)*, 92:1–31, 2011. 1
- [3] Wentao Bao, Qi Yu, and Yu Kong. Evidential deep learning for open set action recognition. In *Proceedings of the IEEE/CVF International Conference on Computer Vision (ICCV)*, pages 13349–13358, 2021. 1
- [4] Fabien Baradel, Romain Brégier, Thibault Groueix, Philippe Weinzaepfel, Yannis Kalantidis, and Grégory Rogez. Posebert: A generic transformer module for temporal 3d human modeling. *IEEE Transactions on Pattern Analysis and Machine Intelligence (TPAMI)*, 45(11):12798–12815, 2022. 1
- [5] John L Barron, David J Fleet, and Steven S Beauchemin. Performance of optical flow techniques. *International Journal of Computer Vision (IJCV)*, 12:43–77, 1994. 2
- [6] Gedas Bertasius, Christoph Feichtenhofer, Du Tran, Jianbo Shi, and Lorenzo Torresani. Learning temporal pose estimation from sparsely-labeled videos. *Advances in Neural Information Processing Systems (NeurIPS)*, 32, 2019. 2
- [7] Joao Carreira and Andrew Zisserman. Quo vadis, action recognition? a new model and the kinetics dataset. In *Proceedings of the IEEE/CVF Conference on Computer Vision and Pattern Recognition (CVPR)*, pages 6299–6308, 2017. 2
- [8] Hanqing Chao, Kun Wang, Yiwei He, Junping Zhang, and Jianfeng Feng. Gaitset: Cross-view gait recognition through utilizing gait as a deep set. *IEEE Transactions on Pattern Analysis and Machine Intelligence (TPAMI)*, 44(7):3467–3478, 2021. 6
- [9] Chen Chen, Roozbeh Jafari, and Nasser Kehtarnavaz. Utdmhad: A multimodal dataset for human action recognition utilizing a depth camera and a wearable inertial sensor. In *Proceedings of the IEEE International Conference on Image Processing (ICIP)*, pages 168–172, 2015. 5
- [10] Junwen Chen, Jie Zhu, and Yu Kong. Atm: Action temporality modeling for video question answering. In *Proceedings of the ACM International Conference on Multimedia (ACM MM)*, pages 4886–4895, 2023. 2
- [11] De Cheng, Xiaojun Chang, Li Liu, Alexander G Hauptmann, Yihong Gong, and Nanning Zheng. Discriminative dictionary learning with ranking metric embedded for person re-identification. In *Proceedings of the International Joint Conference on Artificial Intelligence (IJCAI)*, pages 964–970, 2017. 1
- [12] Chhavi Dhiman and Dinesh Kumar Vishwakarma. View-invariant deep architecture for human action recognition using two-stream motion and shape temporal dynamics. *IEEE Transactions on Image Processing (TIP)*, 29:3835–3844, 2020. 2
- [13] Alexey Dosovitskiy, Philipp Fischer, Eddy Ilg, Philip Hausser, Caner Hazirbas, Vladimir Golkov, Patrick Van Der Smagt, Daniel Cremers, and Thomas Brox. FlowNet: Learning optical flow with convolutional networks. In *Proceedings of the IEEE/CVF International Conference on Computer Vision (ICCV)*, pages 2758–2766, 2015. 2
- [14] Chao Fan, Yunjie Peng, Chunshui Cao, Xu Liu, Saihui Hou, Jiannan Chi, Yongzhen Huang, Qing Li, and Zhiqiang He. Gaitpart: Temporal part-based model for gait recognition. In *Proceedings of the IEEE/CVF Conference on Computer Vision and Pattern Recognition (CVPR)*, pages 14225–14233, 2020. 2
- [15] Chao Fan, Junhao Liang, Chuanfu Shen, Saihui Hou, Yongzhen Huang, and Shiqi Yu. Opengait: Revisiting gait recognition towards better practicality. In *Proceedings of the IEEE/CVF Conference on Computer Vision and Pattern Recognition (CVPR)*, pages 9707–9716, 2023. 6
- [16] Hao-Shu Fang, Jiefeng Li, Hongyang Tang, Chao Xu, Haoyi Zhu, Yuliang Xiu, Yong-Lu Li, and Cewu Lu. Alpha-pose: Whole-body regional multi-person pose estimation

- and tracking in real-time. *IEEE Transactions on Pattern Analysis and Machine Intelligence (TPAMI)*, 45(6):7157–7173, 2022. 1, 8
- [17] David J Fleet and Allan D Jepson. Computation of component image velocity from local phase information. *International Journal of Computer Vision (IJCV)*, 5:77–104, 1990. 1
- [18] João A Francisco and Paulo Sérgio Rodrigues. Computer vision based on a modular neural network for automatic assessment of physical therapy rehabilitation activities. *IEEE Transactions on Neural Systems and Rehabilitation Engineering*, 2022. 1
- [19] Galileo Galilei. Discourses and mathematical demonstrations relating to two new sciences. In *On the Shoulders of Giants: The Great Works of Physics and Astronomy*, pages 515–520. Running Press, 2002. Original work published 1638. 4
- [20] Harshayu Girase, Nakul Agarwal, Chiho Choi, and Kartikeya Mangalam. Latency matters: Real-time action forecasting transformer. In *Proceedings of the IEEE/CVF Conference on Computer Vision and Pattern Recognition (CVPR)*, pages 18759–18769, 2023. 2
- [21] Thiago L Gomes, Renato Martins, João Ferreira, Rafael Azevedo, Guilherme Torres, and Erickson R Nascimento. A shape-aware retargeting approach to transfer human motion and appearance in monocular videos. *International Journal of Computer Vision (IJCV)*, 129(7):2057–2075, 2021. 2
- [22] Yiwen Gu, Shreya Pandit, Elham Saraee, Timothy Nordahl, Terry Ellis, and Margrit Betke. Home-based physical therapy with an interactive computer vision system. In *Proceedings of the IEEE/CVF Conference on Computer Vision and Pattern Recognition Workshops (CVPRw)*, pages 0–0, 2019. 1
- [23] Chuan Guo, Xinxin Zuo, Sen Wang, Xinshuang Liu, Shihao Zou, Minglun Gong, and Li Cheng. Action2video: Generating videos of human 3d actions. *International Journal of Computer Vision (IJCV)*, 130(2):285–315, 2022. 2
- [24] Kaiming He, Georgia Gkioxari, Piotr Dollár, and Ross Girshick. Mask r-cnn. In *Proceedings of the IEEE/CVF International Conference on Computer Vision (ICCV)*, pages 2961–2969, 2017. 2
- [25] Berthold KP Horn and Brian G Schunck. Determining optical flow. *Artificial Intelligence*, 17(1-3):185–203, 1981. 2
- [26] Xiaotao Hu, Zhewei Huang, Ailin Huang, Jun Xu, and Shuchang Zhou. A dynamic multi-scale voxel flow network for video prediction. In *Proceedings of the IEEE/CVF Conference on Computer Vision and Pattern Recognition (CVPR)*, pages 6121–6131, 2023. 1
- [27] Zhaoyang Huang, Xiaoyu Shi, Chao Zhang, Qiang Wang, Ka Chun Cheung, Hongwei Qin, Jifeng Dai, and Hongsheng Li. Flowformer: A transformer architecture for optical flow. In *Proceedings of the European Conference on Computer Vision (ECCV)*, pages 668–685, 2022. 2, 5
- [28] Eddy Ilg, Nikolaus Mayer, Tonmoy Saikia, Margret Keuper, Alexey Dosovitskiy, and Thomas Brox. FlowNet 2.0: Evolution of optical flow estimation with deep networks. In *Proceedings of the IEEE/CVF Conference on Computer Vision and Pattern Recognition (CVPR)*, pages 2462–2470, 2017. 1
- [29] Shihao Jiang, Dylan Campbell, Yao Lu, Hongdong Li, and Richard Hartley. Learning to estimate hidden motions with global motion aggregation. In *Proceedings of the IEEE/CVF International Conference on Computer Vision (ICCV)*, pages 9772–9781, 2021. 6
- [30] Tao Jiang, Peng Lu, Li Zhang, Ningsheng Ma, Rui Han, Chengqi Lyu, Yining Li, and Kai Chen. RtmPose: Real-time multi-person pose estimation based on mmpose. *arXiv preprint arXiv:2303.07399*, 2023. 1
- [31] Yingwei Li, Yi Li, and Nuno Vasconcelos. Resound: Towards action recognition without representation bias. In *Proceedings of the European Conference on Computer Vision (ECCV)*, pages 513–528, 2018. 5
- [32] Rijun Liao, Shiqi Yu, Weizhi An, and Yongzhen Huang. A model-based gait recognition method with body pose and human prior knowledge. *Pattern Recognition (PR)*, 98:107069, 2020. 1
- [33] Beibei Lin, Shunli Zhang, and Xin Yu. Gait recognition via effective global-local feature representation and local temporal aggregation. In *Proceedings of the IEEE/CVF International Conference on Computer Vision (ICCV)*, pages 14648–14656, 2021. 2
- [34] Wei Lin, Muhammad Jehanzeb Mirza, Mateusz Kozinski, Horst Possegger, Hilde Kuehne, and Horst Bischof. Video test-time adaptation for action recognition. In *Proceedings of the IEEE/CVF Conference on Computer Vision and Pattern Recognition (CVPR)*, pages 22952–22961, 2023. 2
- [35] Nikolaus Mayer, Eddy Ilg, Philip Hausser, Philipp Fischer, Daniel Cremers, Alexey Dosovitskiy, and Thomas Brox. A large dataset to train convolutional networks for disparity, optical flow, and scene flow estimation. In *Proceedings of the IEEE/CVF Conference on Computer Vision and Pattern Recognition (CVPR)*, pages 4040–4048, 2016. 1
- [36] Dario Pavllo, Christoph Feichtenhofer, David Grangier, and Michael Auli. 3d human pose estimation in video with temporal convolutions and semi-supervised training. In *Proceedings of the IEEE/CVF Conference on Computer Vision and Pattern Recognition (CVPR)*, pages 7753–7762, 2019. 2
- [37] Yujiang Pu, Xiaoyu Wu, Shengjin Wang, Yuming Huang, Zihao Liu, and Chaonan Gu. Semantic multimodal violence detection based on local-to-global embedding. *Neurocomputing*, 514:148–161, 2022. 1
- [38] Yujiang Pu, Xiaoyu Wu, Lulu Yang, and Shengjin Wang. Learning prompt-enhanced context features for weakly-supervised video anomaly detection. *IEEE Transactions on Image Processing (TIP)*, 2024. 1
- [39] Xuebin Qin, Zichen Zhang, Chenyang Huang, Masood Dehghan, Osmar R Zaiane, and Martin Jagersand. U2-net: Going deeper with nested u-structure for salient object detection. *Pattern Recognition (PR)*, 106:107404, 2020. 5
- [40] Anurag Ranjan, David T Hoffmann, Dimitrios Tzionas, Siyu Tang, Javier Romero, and Michael J Black. Learning multi-human optical flow. *International Journal of Computer Vision (IJCV)*, 128:873–890, 2020. 8
- [41] István Sáradi, Alexander Hermans, and Bastian Leibe. Learning 3D human pose estimation from dozens of datasets using a geometry-aware autoencoder to bridge between

- skeleton formats. In *Proceedings of the IEEE/CVF Winter Conference on Applications of Computer Vision (WACV)*, 2023. 1
- [42] Xiaoyu Shi, Zhaoyang Huang, Weikang Bian, Dasong Li, Manyuan Zhang, Ka Chun Cheung, Simon See, Hongwei Qin, Jifeng Dai, and Hongsheng Li. Videoflow: Exploiting temporal cues for multi-frame optical flow estimation. In *Proceedings of the IEEE/CVF International Conference on Computer Vision (ICCV)*, pages 12469–12480, 2023. 6
- [43] Xiaoyu Shi, Zhaoyang Huang, Dasong Li, Manyuan Zhang, Ka Chun Cheung, Simon See, Hongwei Qin, Jifeng Dai, and Hongsheng Li. Flowformer++: Masked cost volume autoencoding for pretraining optical flow estimation. In *Proceedings of the IEEE/CVF Conference on Computer Vision and Pattern Recognition (CVPR)*, pages 1599–1610, 2023. 2, 6
- [44] Xiuchao Sui, Shaohua Li, Xue Geng, Yan Wu, Xinxing Xu, Yong Liu, Rick Goh, and Hongyuan Zhu. Craft: Cross-attentional flow transformer for robust optical flow. In *Proceedings of the IEEE/CVF Conference on Computer Vision and Pattern Recognition (CVPR)*, pages 17602–17611, 2022. 2, 5, 6
- [45] Shuyang Sun, Zhanghui Kuang, Lu Sheng, Wanli Ouyang, and Wei Zhang. Optical flow guided feature: A fast and robust motion representation for video action recognition. In *Proceedings of the IEEE/CVF Conference on Computer Vision and Pattern Recognition (CVPR)*, pages 1390–1399, 2018. 1
- [46] Shangkun Sun, Yuanqi Chen, Yu Zhu, Guodong Guo, and Ge Li. Skflow: Learning optical flow with super kernels. In *Advances in Neural Information Processing Systems (NeurIPS)*, pages 11313–11326, 2022. 6
- [47] Zachary Teed and Jia Deng. RAFT: Recurrent all-pairs field transforms for optical flow. In *Proceedings of the European Conference on Computer Vision (ECCV)*, 2020. 1, 2, 6
- [48] Torben Teepe, Ali Khan, Johannes Gilg, Fabian Herzog, Stefan Hörmann, and Gerhard Rigoll. Gaitgraph: Graph convolutional network for skeleton-based gait recognition. In *Proceedings of the IEEE International Conference on Image Processing (ICIP)*, pages 2314–2318. IEEE, 2021. 2
- [49] Thomas Unterthiner, Sjoerd Van Steenkiste, Karol Kurach, Raphael Marinier, Marcin Michalski, and Sylvain Gelly. Towards accurate generative models of video: A new metric & challenges. *arXiv preprint arXiv:1812.01717*, 2018. 6, 7
- [50] Christoph Vogel, Konrad Schindler, and Stefan Roth. 3d scene flow estimation with a piecewise rigid scene model. *Proceedings of the IEEE/CVF International Conference on Computer Vision (ICCV)*, 115:1–28, 2015. 1
- [51] Limin Wang, Yuanjun Xiong, Zhe Wang, Yu Qiao, Dahua Lin, Xiaoou Tang, and Luc Van Gool. Temporal segment networks: Towards good practices for deep action recognition. In *Proceedings of the European Conference on Computer Vision (ECCV)*, pages 20–36, 2016. 7
- [52] Zhou Wang, Alan C Bovik, Hamid R Sheikh, and Eero P Simoncelli. Image quality assessment: from error visibility to structural similarity. *IEEE Transactions on Image Processing (TIP)*, 13(4):600–612, 2004. 6, 7
- [53] Syed Talal Wasim, Muhammad Uzair Khattak, Muzammal Naseer, Salman Khan, Mubarak Shah, and Fahad Shah-baz Khan. Video-focalnets: Spatio-temporal focal modulation for video action recognition. In *Proceedings of the IEEE/CVF International Conference on Computer Vision (ICCV)*, 2023. 7
- [54] Philippe Weinzaepfel, Jerome Revaud, Zaid Harchaoui, and Cordelia Schmid. Learning to detect motion boundaries. In *Proceedings of the IEEE/CVF Conference on Computer Vision and Pattern Recognition (CVPR)*, pages 2578–2586, 2015. 1
- [55] Jinbo Xing, Menghan Xia, Yong Zhang, Haoxin Chen, Wangbo Yu, Hanyuan Liu, Xintao Wang, Tien-Tsin Wong, and Ying Shan. Dynamicrafter: Animating open-domain images with video diffusion priors. *Proceedings of the European Conference on Computer Vision (ECCV)*, 2024. 1
- [56] Haofei Xu, Jing Zhang, Jianfei Cai, Hamid Rezaatofghi, and Dacheng Tao. Gmflow: Learning optical flow via global matching. In *Proceedings of the IEEE/CVF Conference on Computer Vision and Pattern Recognition (CVPR)*, pages 8121–8130, 2022. 2, 6
- [57] Yufei Xu, Jing Zhang, Qiming Zhang, and Dacheng Tao. Vit-pose: Simple vision transformer baselines for human pose estimation. *Advances in Neural Information Processing Systems (NeurIPS)*, 35:38571–38584, 2022. 2
- [58] Sijie Yan, Yuanjun Xiong, and Dahua Lin. Spatial temporal graph convolutional networks for skeleton-based action recognition. In *Proceedings of the AAAI Conference on Artificial Intelligence (AAAI)*, 2018. 2, 8
- [59] Jie Yang, Ailing Zeng, Shilong Liu, Feng Li, Ruimao Zhang, and Lei Zhang. Explicit box detection unifies end-to-end multi-person pose estimation. In *Proceedings of the International Conference on Learning Representations (ICLR)*, 2022. 4
- [60] Siyuan Yang, Lu Zhang, Yu Liu, Zhizhuo Jiang, and You He. Video diffusion models with local-global context guidance. In *Proceedings of the International Joint Conference on Artificial Intelligence (IJCAI)*, 2023. 7
- [61] Shuai Yang, Yifan Zhou, Ziwei Liu, and Chen Change Loy. Rerender a video: Zero-shot text-guided video-to-video translation. In *ACM Transactions on Graphics (TOG) – Proceedings of ACM SIGGRAPH Asia*, pages 1–11, 2023. 1
- [62] Zhendong Yang, Ailing Zeng, Chun Yuan, and Yu Li. Effective whole-body pose estimation with two-stages distillation. In *Proceedings of the IEEE/CVF International Conference on Computer Vision*, pages 4210–4220, 2023. 1
- [63] Dingqiang Ye, Chao Fan, Jingzhe Ma, Xiaoming Liu, and Shiqi Yu. Biggait: Learning gait representation you want by large vision models. In *Proceedings of the IEEE/CVF Conference on Computer Vision and Pattern Recognition (CVPR)*, 2024. 2
- [64] Zi Jian Yew and Gim Hee Lee. Rpm-net: Robust point matching using learned features. In *Proceedings of the IEEE/CVF Conference on Computer Vision and Pattern Recognition (CVPR)*, pages 11824–11833, 2020. 4
- [65] Mayssa Zaier, Hazem Wannous, Hassen Drira, and Jacques Boonaert. A dual perspective of human motion analysis-3d pose estimation and 2d trajectory prediction. In *Proceedings of the IEEE/CVF International Conference on Computer Vision (ICCV)*, pages 2189–2199, 2023. 1

- [66] Dingwen Zhang, Guangyu Guo, Dong Huang, and Junwei Han. Poseflow: A deep motion representation for understanding human behaviors in videos. In *Proceedings of the IEEE/CVF Conference on Computer Vision and Pattern Recognition (CVPR)*, pages 6762–6770, 2018. [1](#)
- [67] Yuang Zhang, Jiaxi Gu, Li-Wen Wang, Han Wang, Junqi Cheng, Yuefeng Zhu, and Fangyuan Zou. Mimicmotion: High-quality human motion video generation with confidence-aware pose guidance. *arXiv preprint arXiv:2406.19680*, 2024. [2](#)
- [68] Ziyuan Zhang, Luan Tran, Xi Yin, Yousef Atoum, Xiaoming Liu, Jian Wan, and Nanxin Wang. Gait recognition via disentangled representation learning. In *Proceedings of the IEEE/CVF conference on computer vision and pattern recognition*, pages 4710–4719, 2019. [2](#)
- [69] Mingjun Zhao, Yakun Yu, Xiaoli Wang, Lei Yang, and Di Niu. Search-map-search: a frame selection paradigm for action recognition. In *Proceedings of the IEEE/CVF Conference on Computer Vision and Pattern Recognition (CVPR)*, pages 10627–10636, 2023. [2](#)
- [70] Qi Zhao, Shijie Wang, Ce Zhang, Changcheng Fu, Minh Quan Do, Nakul Agarwal, Kwonjoon Lee, and Chen Sun. Antgpt: Can large language models help long-term action anticipation from videos? *Proceedings of the International Conference on Learning Representations (ICLR)*, 2024. [2](#)
- [71] Ce Zheng, Sijie Zhu, Matias Mendieta, Taojiannan Yang, Chen Chen, and Zhengming Ding. 3d human pose estimation with spatial and temporal transformers. In *Proceedings of the IEEE/CVF Conference on Computer Vision and Pattern Recognition (CVPR)*, pages 11656–11665, 2021. [1](#)
- [72] Jinkai Zheng, Xinchun Liu, Shuai Wang, Lihao Wang, Chenggang Yan, and Wu Liu. Parsing is all you need for accurate gait recognition in the wild. In *Proceedings of the ACM International Conference on Multimedia (ACM MM)*, pages 116–124, 2023. [2](#)
- [73] Shuai Zheng, Junge Zhang, Kaiqi Huang, Ran He, and Tieniu Tan. Robust view transformation model for gait recognition. In *Proceedings of the IEEE International Conference on Image Processing (ICIP)*, pages 2073–2076, 2011. [5](#)
- [74] Kun Zhou, Xiaoguang Han, Nianjuan Jiang, Kui Jia, and Jiangbo Lu. Hemlets pose: Learning part-centric heatmap triplets for accurate 3d human pose estimation. In *Proceedings of the IEEE/CVF International Conference on Computer Vision (ICCV)*, pages 2344–2353, 2019. [1](#)
- [75] Wentao Zhu, Xiaoxuan Ma, Zhaoyang Liu, Libin Liu, Wayne Wu, and Yizhou Wang. Motionbert: A unified perspective on learning human motion representations. In *Proceedings of the IEEE/CVF International Conference on Computer Vision (ICCV)*, pages 15085–15099, 2023. [2](#), [8](#)
- [76] Xizhou Zhu, Yujie Wang, Jifeng Dai, Lu Yuan, and Yichen Wei. Flow-guided feature aggregation for video object detection. In *Proceedings of the IEEE/CVF International Conference on Computer Vision (ICCV)*, pages 408–417, 2017. [1](#)
- [77] Zheng Zhu, Xianda Guo, Tian Yang, Junjie Huang, Jiankang Deng, Guan Huang, Dalong Du, Jiwen Lu, and Jie Zhou. Gait recognition in the wild: A benchmark. In *Proceedings of the IEEE/CVF International Conference on Computer Vision (ICCV)*, pages 14789–14799, 2021. [1](#)



# H-MoRe: Learning Human-centric Motion Representation for Action Analysis

## Supplementary Material

### A. Appendix

#### A.1. Adaptive Edge Detection from Flow Maps

In Sec. 3.2.2, to refine motion details and incorporate shape information, we build boundary constraint based on human boundaries and edges of flow maps. The human boundaries are detected using a Canny operator. However, the edges of the flow map cannot be extracted using simple operators like the Canny operator. Therefore, we designed an edge detection method with learnable thresholds specifically for flow maps. We define the edges of a flow map  $M$  as a series of discrete points, meaning that these points exhibit either intensity or angular discontinuities relative to their neighboring points. Intensity discontinuities indicate significant differences in offset magnitude between a point  $i$  and its neighbors  $j$ , *e.g.*, the boundary between a moving foreground and a static background. This can be mathematically expressed as:

$$s_I = \{i \in M \mid |||M_i||| - |||M_j||| \geq \vartheta_i\}, \quad (10)$$

where  $\vartheta_i$  represents the learnable intensity threshold. On the other hand, angular discontinuities refer to situations where the angle of the offset between  $i$  and  $j$  exhibits a significant difference, often occurring between different body patterns. This can be represented as:

$$s_A = \left\{i \in M \mid \frac{M_i \cdot M_j}{|||M_i||| \cdot |||M_j|||} \geq \vartheta_a\right\}, \quad (11)$$

where  $\vartheta_a$  represents the learnable angular threshold. Therefore, for any flow map  $M$ , its edge map  $s$  can be formulated as the union of intensity and angular discontinuities:

$$s = s_I \cup s_A. \quad (12)$$

#### A.2. Patch-Centroid Distance Validation

In Eq. (8), we propose a method to approximate the Chamfer distance using the patch-centroid distance. Here, we provide some validations for this approximation. Based on the following formulation, the Chamfer distance can be approximately transformed, as shown below, under the condition of sufficient curve smoothness, leading to the theoretical conclusion presented in the main text:

$$\begin{aligned} \mathcal{C}(\mathcal{P}_s, \mathcal{P}_e) &= \frac{1}{n_p} \sum_{\{i, \hat{j}\}} \mathcal{D}(i, \hat{j}) \\ &\approx \mathcal{D} \left[ \frac{1}{n_p} \sum_{\{i, \hat{j}\}} i, \frac{1}{n_p} \sum_{\{i, \hat{j}\}} \hat{j} \right] \\ &\approx \mathcal{D}(\mathcal{CP}_s, \mathcal{CP}_e). \end{aligned} \quad (13)$$



Figure 10. **Edges of flow map.** Through the complementarity of intensity and angular edges (highlighted in the red box), we can effectively detect the edges present in the flow map.



Figure 11. **Validation for patch-centroid distance.** By using the patch-centroid distance as the sole loss function, we can effectively train a network to deform one curve into another by applying an estimated morph.

Apart from the theoretical validation, we also conduct experiments on the MNIST dataset to verify whether the proposed patch-centroid distance can effectively measure the distance between two curves. As shown in Fig. 11, in the experiment, a network tries to apply a non-rigid transformation (Morph) to a moving image (Moving) to generate a moved image (Moved), aligning it with a specified target image (Target). By using the patch-centroid distance as the sole loss function to measure the curve distance between the moved and target images, the network successfully converges. This experimental result further demonstrates the patch-centroid distance as an effective approximation of the Chamfer distance.

#### A.3. Evaluating Action Recognition with TSN

Similar to Sec. 4.1, besides the results shown in Tab. 2, we also validate the improvement in real-time motion analysis performance achieved by H-MoRe on the action recognition task. Following the same experimental setup as described in Sec. 4.2, we conducted a quantitative comparison on the Diving48 dataset using TSN instead of Video-FocalNets as the action recognition classifier. To validate the improvement in real-time motion analysis performance achieved by H-MoRe, we conducted a quantitative comparison on the Diving48 dataset using TSN as the action recognition classifier. As shown in Tab. 6, compared to using optical flow as the motion representation input, using H-MoRe as the input significantly improved classification performance. This further demonstrates the effectiveness of H-MoRe in real-time scenarios. Besides, due to the use of additional output

Methods	Acc@1↑	Acc@5↑	Params (M)
w/o Flow	65.58	95.18	4.5
RAFT	66.09	93.45	4.6 + 5.25
GMA	69.54	94.77	4.6 + 5.88
GMFlow	70.91	95.89	4.6 + 4.68
CRAFT	70.20	95.74	4.6 + 6.30
SKFlow	67.26	94.57	4.6 + 6.27
VideoFlow	<u>71.07</u>	<u>96.80</u>	4.6 + 12.65
FlowFormer++	70.66	95.94	4.6 + 16.15
<b>H-MoRe Ours</b>	<b>72.69</b>	<b>97.60</b>	4.7 + 5.57

Table 6. **Quantitative comparison for action recognition in real-time scenarios.** Alongside with numbers of learnable parameters in whole recognition pipeline containing motion estimation networks and classifiers.

channels (optical flow: 2 more channels; H-MoRe: 4 more channels), the number of parameters in classifiers fluctuates slightly compared to the vanilla TSN. However, this does not affect performance. We have also indicated these fluctuations in the tables (Params).

#### A.4. Skeleton Map Alignment Methods

In Sec. 3.3, we mentioned that to impose a skeleton constraint on the local flow  $M_t$ , the original skeleton constraint  $\mathcal{F}$  needs to be transformed to  $\mathcal{F}'$ . This is because the  $\tilde{\mathbf{K}}$  used in  $\mathcal{F}$  represents the skeleton’s offset relative to the environment rather than relative to the subject itself. Therefore, we need to compute the skeleton offset relative to the subject itself by aligning the skeleton map  $\mathbf{K}_{t+1}$  from frame  $\mathbf{X}_{t+1}$  to  $\mathbf{K}_t$  from  $\mathbf{X}_t$ . In practice, we applied two different alignment methods: (i) full-body and (ii) head-anchor. Full-body alignment aligns  $\mathbf{K}_{t+1}$  by solving the following equation using the least squares method:

$$H' = \arg \min_H \|H \times \mathbf{K}_{t+1} - \mathbf{K}_t\|, \quad (14)$$

$$\mathbf{K}'_{t+1} = H' \times \mathbf{K}_{t+1}.$$

Here,  $H$  is a homography matrix, which enables skeleton map alignment through projection. This method is suitable for scenarios where the human body does not undergo rotation, such as in gait recognition or video generation.

However, when body rotation occurs, as in diving scenarios, full-body alignment based on all skeletal points may lead to errors in motion estimation. To address this, we use head-anchor alignment. This method employs an affine transform to rotate and scale  $\mathbf{K}_{t+1}$ , ensuring the head regions in the skeleton maps at the two time points are closely matched. Based on this alignment, we obtain the transformed  $\mathbf{K}'_{t+1}$ .

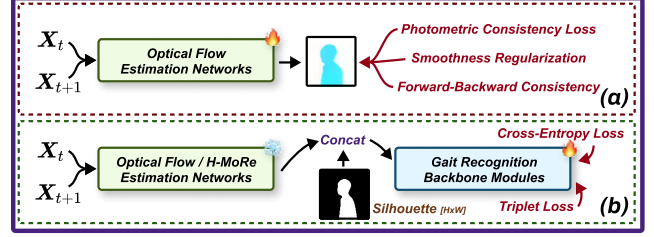


Figure 12. **Pipeline for gait recognition experiments.** (a) illustrates how we fine-tune the optical flow estimation networks. (b) demonstrates how motion information is integrated into the gait recognition pipeline.

### A.5. Details of Experimental Settings

In Sec. 4, we compare the accuracy of H-MoRe in representing motion against optical flows across three tasks. In this subsection, we provide detailed explanations and additional information about our experimental workflow.

#### A.5.1. Gait Recognition

For the gait recognition task, we first extract 2,800 sequences from the CASIA-B training set to fine-tune the optical flow estimation models (Fig. 12 (a)) and train our H-MoRe as denoted in Sec. 3.3. After fine-tuning and training, the parameters of these motion estimation networks are frozen. We then use these models as inputs to train classifiers, specifically GaitBase or GaitSet networks with identical structures (Fig. 12 (b)).

Since silhouettes are the default input for gait recognition and require a single-channel input, we adjust the input layer of the classifier for optical flow (2 channels) to support three-channel input. For H-MoRe, which includes world flow (2 channels) and local flow (2 channels), we use a five-channel input. During this stage, only the classifier’s parameters are trained. After training, all parameters are fixed, and the models are then tested on the testing set, producing the results shown in Tab. 1.

#### A.5.2. Action Recognition

For the action recognition task, we similarly extract 14,000 sequences from the Diving48 training set to fine-tune the optical flow estimation models and train H-MoRe (Fig. 12 (a)). After freezing the parameters of these motion estimation networks, we train downstream classifiers: Video-FocalNets (Tab. 2) and TSN (Tab. 6).

For each moment, RGB images, which are the default input for action recognition, are combined with optical flow or H-MoRe and fed into the classifier. Specifically, these inputs are either (RGB 3 channels + Optical Flow 2 channels) or (RGB 3 channels + H-MoRe 4 channels).

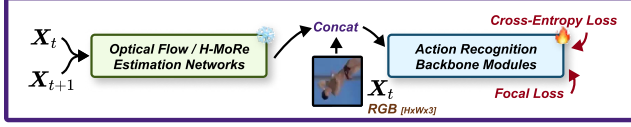


Figure 13. **Pipeline for action recognition experiments.** Similar to the gait recognition pipeline, the main difference lies in using RGB frames as additional input instead of silhouettes.

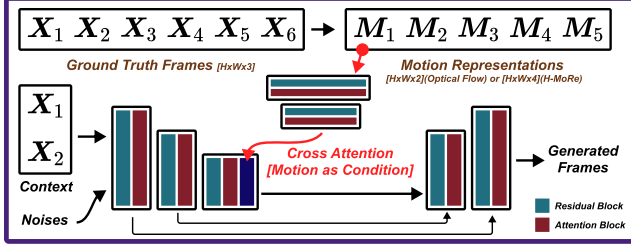


Figure 14. **Pipeline for video generation experiments.** This figure illustrates how we use motion representations as conditions for the video generation model to guide video reconstruction. For more details on the network structure, please refer to the LGC-VD.

### A.5.3. Video Generation

Our video generation tasks in the main text can be regarded as motion-guided video reconstruction tasks. Unlike the first two tasks, this task is designed to directly evaluate the accuracy of motion provided by H-MoRe. Here, we use the motion at each time step as a condition for a diffusion model to reconstruct the original video. This implies that ignoring lighting variations, the SSIM and FVD scores in Tab. 2 are highly correlated with the accuracy of the motion information provided by optical flow and H-MoRe.

We fine-tune the optical flow estimation models and train H-MoRe using 600 sequences from the UTD-MHAD dataset, then freeze their parameters. Notably, unlike the pipelines in the previous tasks, this task does not concatenate motion directly with input (the first two frames of the sequence). Instead, the motion is used as a condition and integrated into the diffusion models via cross-attention (Fig. 14).

These three tasks collectively demonstrate the effectiveness of H-MoRe in providing accurate motion information, either indirectly (gait recognition and action recognition) or directly (video generation). Additionally, Fig. 7 in the main text and attached video provide a more intuitive visual comparison between our H-MoRe and optical flow, highlighting their respective differences and characteristics.

## B. Variables

In the following table, we summarize the symbols used in the main text, along with their detailed definitions and rep-

resentations.

Variables	Description	Type [shape]
$M_w$	<b>H-MoRe’s world flow.</b> It represents the offset of each body point relative to the environment, <i>e.g.</i> , the ground or the camera.	Matrix [ $H \times W \times 2$ ]
$M_l$	<b>H-MoRe’s local flow.</b> It represents the offset of each body point relative to the subject themselves.	Matrix [ $H \times W \times 2$ ]
$X_t X_{t+1}$	<b>Two consecutive frames.</b> They are usually two frames from a video, spaced more than 0.1 seconds apart.	Matrix [ $H \times W \times 3$ ]
$K_t K_{t+1}$	<b>Skeleton maps.</b> They represent a series of (210) skeletal points of a person in frames $X_t$ and $X_{t+1}$ , with each point containing coordinates and visibility information ( $c$ ).	Matrix [ $210 \times 3$ ]
$\vec{K}$	<b>Skeleton offsets.</b> It represents the offset of each point in the skeleton map between two time steps, <i>i.e.</i> , $K_{t+1} - K_t$ .	Matrix [ $210 \times 3$ ]
$e$	Human boundaries.	Curve
$s$	Edges of flow map.	Curve
$\mathcal{P}_e$	Human boundaries within patch $\mathcal{P}$ .	Curve
$\mathcal{P}_s$	Edges of flow map within patch $\mathcal{P}$ .	Curve
$p$	Any point within the human body in the flow maps.	Point
$\hat{q}$	The closest point within skeleton offsets $\vec{K}$ with the highest visibility towards $p$ .	Point
$i$	Any point on the edges of flow map $s$ .	Point
$\hat{j}$	The nearest point within human boundaries $e$ towards $i$ .	Point
$c_{\mathcal{P}_e}$	The centroid of curve $\mathcal{P}_e$ .	Point
$c_{\mathcal{P}_s}$	The centroid of curve $\mathcal{P}_s$ .	Point
$v_s$	<b>Subject motion.</b> It represents the overall motion trend of subjects.	Vector [ $\Delta x, \Delta y$ ]
$u_p$	The estimated flow $M$ at point $p$ .	Vector [ $\Delta x, \Delta y$ ]
$k_{\hat{q}}$	The skeleton offset $\vec{K}$ at point $\hat{q}$ .	Vector [ $\Delta x, \Delta y$ ]
$\Phi$	<b>H-MoRe’s network component.</b> It estimates world flow $M_w$ between consecutive frames $X_t$ and $X_{t+1}$ .	Network [Params: $\approx 3.4M$ ]
$\Psi$	<b>H-MoRe’s network component.</b> It estimates subject motion $v_s$ based on world flow $M_w$ .	Network [Params: $\approx 2.1M$ ]
$\mathcal{F}$	<b>Our skeleton constraint.</b> It ensures that each body point’s movement adheres to kinematic constraints.	Function
$\mathcal{G}$	<b>Our boundary constraint.</b> It aligns human shapes onto our estimated flow maps.	Function
$\mathcal{F}_A$	<b>Angular constraint.</b> Component of skeleton constraint.	Function
$\mathcal{F}_I$	<b>Intensity constraint.</b> Component of skeleton constraint.	Function
$\mathcal{C}$	Chamfer distance between two curves.	Function
$\mathcal{D}$	Euclidean distance between two points.	Function
$\omega_1$	Learnable parameters in $\Phi$ .	Parameters
$\omega_2$	Learnable parameters in $\Psi$ .	Parameters
$\vartheta_a$	Threshold for angular constraint $\mathcal{F}_A$ .	Constant
$\vartheta_l^l \vartheta_l^h$	Low and high boundary threshold for intensity constraint $\mathcal{F}_I$ .	Constant

Table 7. **Symbols used in the main text.** Additionally, the description includes its relevant information.